Available online at www.sciencedirect.com
ScienceDirect
Trans. Nonferrous Met. Soc. China 34(2024) 347−360
Transactions of Nonferrous Metals Society of China
www.tnmsc.cn

Melting and separation behaviors of electric arc furnace dust pellets under iron bath conditions

Chao YANG[1], Xue-feng SHE[1], Ru-yi WANG[2], Jing-song WANG[1], Qing-guo XUE[1]

1. State Key Laboratory of Advanced Metallurgy, University of Science and Technology Beijing, Beijing 100083, China;
2. Research Institute, Baoshan Iron & Steel Co., Ltd., Shanghai 201900, China

Received 26 June 2022; accepted 14 March 2023

Abstract: To enhance the utilization capacity of zinc-containing electric arc furnace dust (EAFD), the reduction melting behavior of EAFD under iron bath conditions was empirically investigated. The sphericity of Fe droplets was defined as the judgment criterion for its coalescence, and then, the relationship between iron droplet diameter and sphericity was determined over time. The behavior of melting and separation of EAFD pellets was also established based on the experiments. The results showed that the Zn removal rate of EAFD pellets under iron bath conditions reached more than 99% at 5.0 min, but the metal−slag separation was not finished at 15.0 min. Due to the compositional fluctuation, several regions of liquid slag were formed in the EAFD pellets, and then, the liquid slag grew until the pellets melted completely. The number of Fe droplets with sphericity >65% and diameter >500 μm decreased with time, and large-diameter Fe droplets were the first to undergo complete separation. The separation process of slag and iron involved the initial formation of Fe droplets via Brownian motion, followed by an increase in the diameter of the iron droplets via the Marangoni effect. The Fe droplets in the slag phase drop rate resembled Stokes Law.
Key words: electric arc furnace dust; iron bath; pellet melting; melt−slag separation

1 Introduction

Steel production generates large amounts of steel dust, which is emitted from furnaces with exhaust gases, especially in processes that use scrap as the main raw material [1]. As a representative type of steel plant dust, electric arc furnace dust (EAFD) has an output of about 1%−2% of the charge in a typical electric arc furnace operation [2,3]. In 2020, global crude steel production reached 1.876 billion tons. Among the total steel produced, 26.3% is produced using electric arc furnaces, which produce 50−100 million tons of EAFD annually worldwide. EAFD contains about 30% zinc as zincite and franklinite, and 15%−50% iron as magnetite, franklinite, and hematite. Thus, the conversion of EAFD into a valuable resource for producing recycled zinc and iron is urgently needed [4−9].

Among all high-temperature metal recovery processes used for recycling EAFD, the Waelz kiln process accounts for about 75% of the total treated EAFD globally [2,10]. During the Waelz kiln process, first, a homogeneous mixture of EAFD, reductant, and flux is pelletized. Then, the pelletized material is sent into the Waelz kiln for drying and preheating using the countercurrent-flow kiln gas. Finally, the metal oxides are reduced at about 1100−1200 °C to volatilize zinc from the charge in the form of metal vapors. By controlling the admission of air at the kiln outlet end, zinc in

Corresponding author: Xue-feng SHE, Tel/Fax: +86-10-62334444, E-mail: shexuefeng@ustb.edu.cn
DOI: 10.1016/S1003-6326(23)66403-9

the gas phase was oxidized again and formed as Waelz oxide [11−13]. Although the Waelz kiln process is a relatively mature process for recycling EAFD, it has several disadvantages, including (1) low productivity, (2) low ZnO content of the produced zinc-rich dust, (3) high maintenance costs, (4) massive residue generation (approximately 700−800 kg/t of the raw material dust), and (5) insufficiently enriched Fe [14−17].

Other processes, such as rotary hearth furnaces, Primus, OxyCup, Oxyfines, and Ausmelt, are designed to recover zinc and iron from the EAFD. However, no process can recover zinc and iron at the same time economically and efficiently [18−20]. A novel electric melting reduction furnace (ESRF) process was developed to resolve the above setbacks [21]. In the ESRF process, only electrical energy is used to produce extremely high temperatures. During the ESRF process, the EAFD is completely melted at high temperatures. Its core equipment is an electric arc furnace that does not need fossil fuels to provide heat energy. Also, the ESRF process provides various schemes to recover reduced high-vapor-pressure metals, such as zinc and lead, as well as alkali metal chlorides [14].

LIU et al [22] and ZHU et al [23] reported the reduction of Zn-containing dust using the iron bath method and found that the Zn removal rate of the EAFD under iron bath conditions was above 98%, and the ZnO content of the Zn-rich powder was over 87%. LEUCHTENMÜELLER et al [24] studied the kinetics of the combined carbothermic and metallothermic reduction of ZnO in a metal bath and found that the temperature-dependent contribution of the metallothermic zinc oxide reduction was between 25% and 50% of overall reaction mechanism, and the zinc recovery was >99.9%. However, studies on the behavior during the melt reduction process are limited and need to be explored thoroughly. Thus, in this study, EAFD was pelletized and heated under the iron bath conditions to study the reduction, melting, and separation behavior of EAFD. This study might provide a theoretical basis for the efficient recovery of zinc-containing EAFD. And the findings of this study might have a positive effect on understanding slag−iron separation in non-blast furnace iron-making processes.

2 Experimental

2.1 Raw materials

The EAFD used in the experiments was supplied by a steel plant in China, and the typical chemical composition is given in Table 1. The reducing agent used was graphite powder (99.95%), and SiO_2 (99%) was used as the flux.

Table 1 Compositional analysis of EAFD (wt.%)

Zn	Fe	Mn	Pb	Mg	Al
35.5	15.0	1.66	1.57	1.35	0.40
Si	Ca	S	Cl	O	
1.60	4.84	0.83	6.50	23.2	

The EAFD was dried and ground into a powder of less than 0.074 mm and then subjected to X-ray diffraction (XRD, model SMARTLAB (9), Rigaku Corporation, Japan). The results are shown in Fig. 1. Zinc existed not only in the metal oxide (ZnO) form but also in the form of franklinite ($ZnFe_2O_4$). And Fe existed in the form of magnetite (Fe_3O_4) and $ZnFe_2O_4$, which matched the findings of a previous study [25].

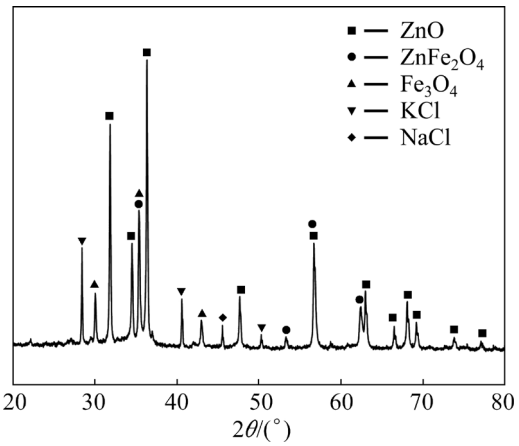

Fig. 1 XRD pattern of EAFD

2.2 Experimental principle

The phase diagram of the MgO−CaO−SiO_2−Al_2O_3 (Al_2O_3 content of 5 wt.%) system was calculated using FactSage 8.0, and the results are shown in Fig. 2. The binary basicity (R=n(CaO)/n(SiO_2)) was 0.9, the melting point of the slag phase was less than 1400 °C. And the slag phase properties did not change much when the slag phase composition was slightly changed. The

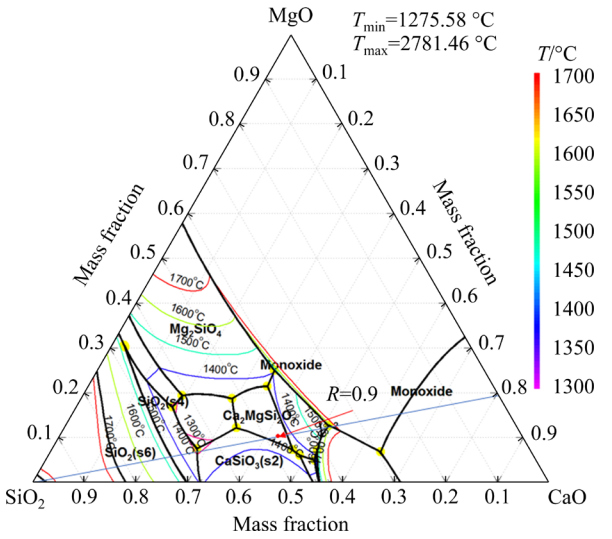

Fig. 2 MgO−CaO−SiO_2−Al_2O_3 quaternary phase diagram (Al_2O_3 content of 5 wt.%)

amount of slagging agent was determined according to the Ca and Si content in Table 1 and R.

The Zn removal rate (η_{Zn}) was calculated using the formula (Eq. (1)) as follows:

$$\eta_{Zn}=\frac{m_{Zn,b}-m_{Zn,a}}{m_{Zn,b}}\times 100\% \quad (1)$$

where $m_{Zn,b}$ and $m_{Zn,a}$ are the masses of elemental Zn in the pellet before and after the reaction, respectively.

The Fe removal rate (η_{Fe}) was calculated using the formula (Eq. (2)) as follows:

$$\eta_{Fe}=\frac{m_{Fe,b}-m_{Fe,a}}{m_{Fe,b}}\times 100\% \quad (2)$$

where $m_{Fe,b}$ and $m_{Fe,a}$ are the masses of Fe in the pellet before and after the reaction, respectively.

2.3 Experimental procedure and apparatus

In the iron bath method, pellets were added to the hot metal to study the reduction, melting, and separation processes of EAFD pellets. First, the mixture of 10 g EAFD, 0.41 g SiO_2, and 1.23 g carbon was compacted into a pellet (20 mm in diameter and 14 mm in height). Then, the pellet was dried at 105 °C for 8 h using a drying oven in an air atmosphere. Then, 100 g of pig iron powder was added to the graphite crucible (30 mm in inner diameter and 75 mm in depth), and then the graphite crucible was placed inside the high-temperature electric resistance furnace using crucible tongs. When the furnace was heated to the test temperature (1500 °C), the pig iron melted and was kept warm for 30 min. Finally, the dried pellets were added to the iron bath using an iron wire. After the required reaction time, the crucible was removed and quenched. The ambient gas in the furnace was air, and the reaction time selected for this experiment was 5.0, 7.5, 10.0, 12.5, and 15.0 min. The samples were characterized using the methods described below.

The chemical composition of the slag samples was determined using an X-ray fluorescence (XRF, model AxiosmAX, PANalytical B.V., Netherland) spectrometer, and the content of C in the slag phase was analyzed using a carbon−sulfur analyzer (model CS−2800, NCS Testing Technology Co., Ltd., China). Then, XRD (model SMARTLAB (9), Rigaku Corporation, Japan) was used to confirm the phase of the slag. Scanning electron microscopy (SEM, model Quanta250, FEI, USA) and energy-dispersive X-ray spectroscopy (EDS) were performed to investigate the morphology of slag samples. Additionally, the spatial distribution [26] of iron droplets in the slag was determined using X-ray transmission computed tomography (XCT, model FF35CT, YXLON, Germany). The flowcharts of experimental preparation and detection are shown in Fig. 3.

3 Results and analysis

3.1 Recovery ratio of Zn-containing EAFD

The chemical compositions of the EAFD before and after melting separation are given in Table 2. At 5.0 min, the residual amount of ZnO in the slag was 0.02 wt.%. The Zn removal rate at 5.0 min was calculated using Eq. (2), which reached more than 99%; these findings matched those of another study [24]. The Zn content in the slag was almost undetectable at 12.5 min. The metal−slag separation process was not complete at 15.0 min, and thus, the Fe content in the slag was high. The reaction mechanisms describing the high-temperature reduction of ZnO, $ZnFe_2O_4$, and FeO with carbon or CO are shown in Reactions (3)−(9):

$$ZnO(s)+C(s)=Zn(g)+CO(g) \quad (3)$$

$$ZnFe_2O_4(s)+C(s)=Zn(g)+Fe_2O_3(s)+CO(g) \quad (4)$$

$$Fe_2O_3(s)+3C(s)=2Fe(l)+3CO(g) \quad (5)$$

$$ZnO(s)+CO(g)=Zn(g)+CO_2(g) \quad (6)$$

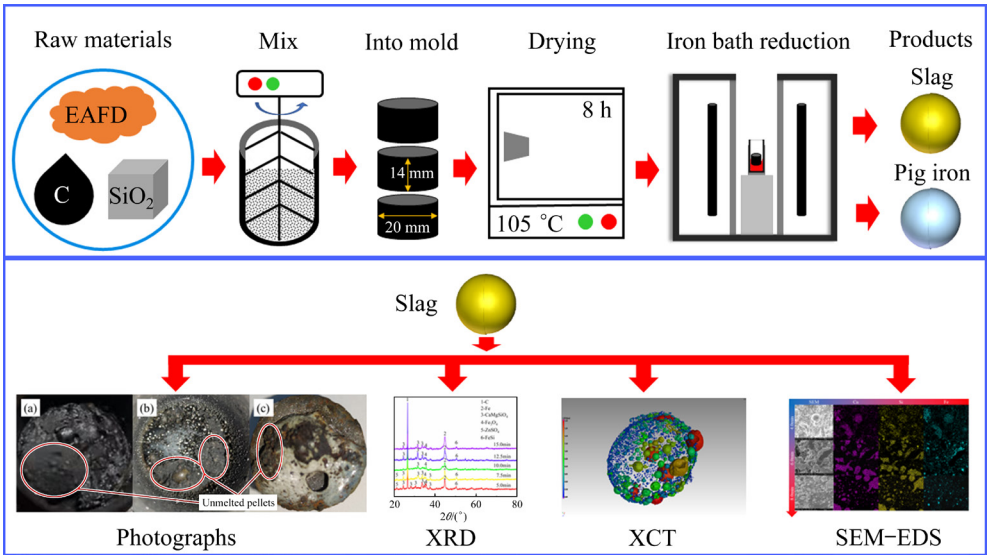

Fig. 3 Flow charts of experimental preparation and detection

Table 2 Chemical composition of slag phase at different melting time (wt.%)

Melting time/min	C	Fe	Zn	Si	Ca	Mg	Al	O
0	10.69	12.50	31.71	4.80	4.32	1.21	0.36	20.72
5.0	4.38	30.60	0.02	9.39	9.94	0.00	2.20	34.33
7.5	4.63	25.85	0.01	8.96	11.06	5.40	1.83	35.67
10.0	4.23	17.91	0.01	12.74	12.35	5.29	3.09	37.73
12.5	5.17	25.98	0.00	9.24	10.34	5.06	2.44	35.85
15.0	5.91	22.58	0.00	9.71	12.68	5.66	2.26	36.80

$$ZnFe_2O_4(s)+CO(g)=Zn(g)+Fe_2O_3(s)+CO_2(g) \quad (7)$$

$$Fe_2O_3(s)+3CO(g)=2Fe(l)+3CO_2(g) \quad (8)$$

$$C(s)+CO_2(g)=2CO(g) \quad (9)$$

The effect of melting time on the Zn and Fe removal rates is shown in Fig. 4. The Zn removal rate was more than 99% at 5.0 min, and no change was detected in the Zn removal rate with an increase in the melting time. The Fe removal rate initially showed an increasing trend with time up to 10.0 min, then decreased at 12.5 min and again increased at 15.0 min. The incomplete melting of the pellet in the iron bath might be one of the reasons for the increasing trend of Fe removal rate up to 10.0 min. Also, the reduced Fe droplets were separated from the slag phase but did not enter the iron bath for up to 10.0 min, which was not detected in the slag phase. Thus, the Fe removal rate appeared to be higher at 10.0 min. At 12.5 min, the pellets were completely melted in the iron bath, and a large number of Fe droplets were found in the slag, which resulted in a reduction in the Fe removal rate. The Fe removal rate increased with the increase in melting time after the complete melting of the pellets in the iron bath at 12.5 min. This occurred because as melting time increased, the melt−slag separation time increased, the separation became better, and the iron content in the slag phase decreased.

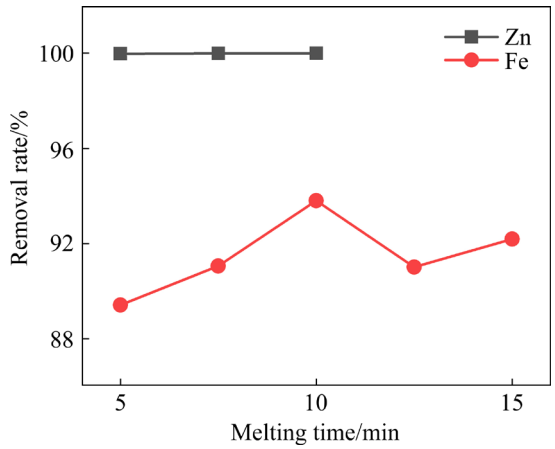

Fig. 4 Effect of melting time on Zn and Fe removal rates

The XRD patterns of molten slag at different melting time are shown in Fig. 5. It was found that C, Fe, FeSi, the calcium-magnesium silicate phase, Fe_3O_4, and $ZnSO_4$ were present in the slag at melting time of 5.0 min. At 10.0 min, the diffraction peak of $ZnSO_4$ almost disappeared, and the diffraction peak of Fe became weaker. This was caused by the continuous removal of ZnO and Fe

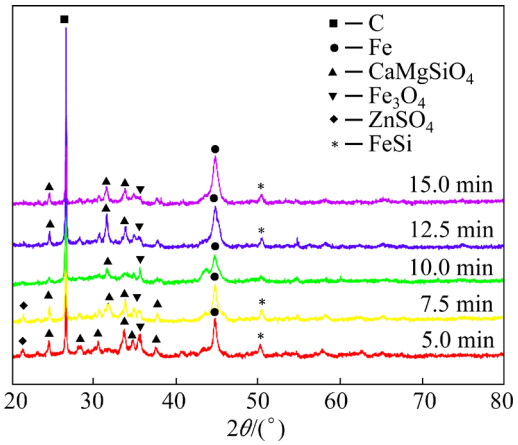

Fig. 5 XRD patterns of slag phase at different melting time

from the slag with an increase in the melting time. The diffraction peak of Fe was enhanced at melting time of 15.0 min due to the increased Fe content in the slag phase at this melting time. Thus, there was a strong C diffraction peak in the XRD patterns of the slag phase at all melting time, which reflected higher C content in the slag phase and was consistent with the compositional analysis given in Table 2.

3.2 Melting behavior of pellets in iron bath

The melting behavior of the pellets was determined by observing the pellets in the iron bath at different melting time. The photographs of the pellets are shown in Fig. 6. When the melting time was 5.0 min, the pellets were mostly unmelted and round, floating on the surface of the iron bath. The number of unmelted pellets gradually decreased with the progress of reduction (increase in melting time). When the melting time was 10.0 min, most of the pellets were melted to form the slag, and a small number of unmelted pellets were gathered in powder form on the slag side.

The melting result of the pellets in the iron bath at melting time of 7.5 min was studied, and the photograph is shown in Fig. 7. The liquid slag phase was formed in the lower part of the pellet, while the upper part of the pellet kept the original shape of the pellet at 7.5 min. Many yellow-brown spots were present on the unmelted pellets. The spots were related to the slag phase formed via the slagging reaction of the pellets. The compositional fluctuation in the pellets after mixing was the main reason for the occurrence of slagging reaction in the unmelted pellets. The slag phase gradually expanded with the melting time, which was formed continuously around the liquid slag due to the occurrence of slagging reaction.

The melting behavior of the pellets was observed after quenching at different melting time, i.e., 4.0, 6.0, and 8.0 min, and the results are shown in Fig. 8. The pellets were incompletely melted after 8.0 min in the absence of an iron bath, and the pellets kept their original shape in the graphite crucible. The shape of the unmelted pellets became loose as the melting time increased from 4.0 to 8.0 min, while an obvious spherical slag phase was observed in the upper part of the pellets at 8.0 min. The liquid slag phase in the pellet produced spheres under surface tension. Also, there were multiple slag phase spheres in the pellet, which were formed at the multiple compositional fluctuation sites in the pellet. Some slag phase spheres were present inside or at the edge of the pellet, where slagging reactions could occur to form liquid slag.

SEM was performed on the interior of the unmelted pellets to study the microscopic morphological changes during the melting of the

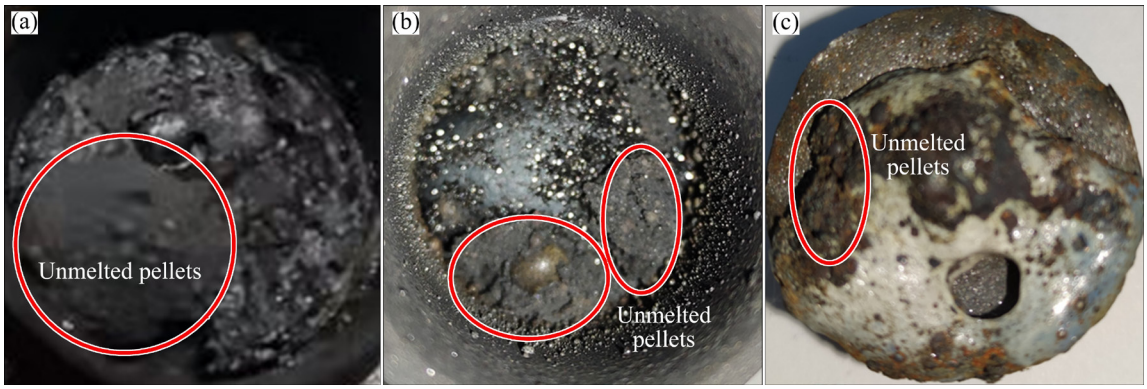

Fig. 6 Photographs of pellets in iron bath at different melting time: (a) 5.0 min; (b) 7.5 min; (c) 10.0 min

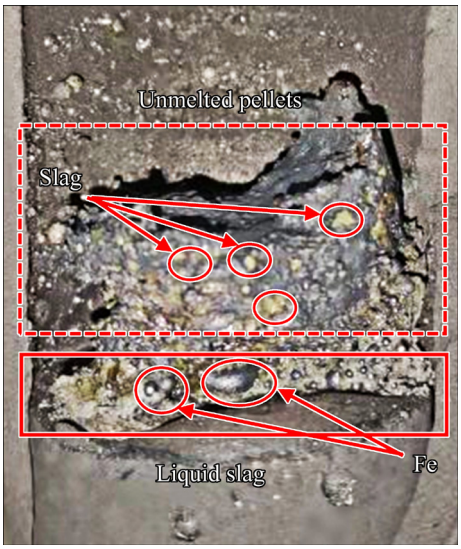

Fig. 7 Photograph of unmelted pellets after melting for 7.5 min

pellets, and the results are shown in Fig. 9. The slag phase was formed inside the pellets at different melting time, and multiple slag phase regions were created. The slag phase contained a large amount of elemental Fe at 4.0 min. This occurred because the reduction of Fe_2O_3 to FeO promoted the slagging reaction, resulting in the lowering of the melting point of the slag phase and the formation of liquid slag. The distribution of Fe began to concentrate at the edge of the slag phase at 6.0 min. This was because the concentration of Fe at the edge of the slag phase increased with the reaction time due to a decrease in FeO to metal Fe. Fe was mainly concentrated around Ca and Si at 8.0 min. The effective metal−slag separation at a prolonged melting time was responsible for the concentration of Fe around Ca and Si. The smaller-diameter particles in the slag were spherical, and the larger-diameter particles in the slag were shaped irregularly. This indicated that the slag phase formed in the pellet initially had a spherical shape under surface tension, while during melting, the shape of the slag phase became irregular due to the coalescence of multiple slag phases during spreading growth.

3.3 Motion behavior of Fe droplets in molten slag

The scanning electron micrographs of the metal−slag interface at different melting time are shown in Fig. 10. At 5.0 min (Fig. 10(a)), millimeter-sized molten iron appeared at the slag−iron interface, accompanied by many iron droplets having a diameter less than 100 μm, most of which were distributed in the center of the slag phase. At 7.5 min (Fig. 10(b)), the number of Fe droplets with a diameter less than 100 μm at the metal−slag interface was decreased, and the Fe droplets were concentrated at the edge of the slag phase. This might have occurred because of the gradual growth of Fe droplets with the melting time and their tendency to move toward the edge of the slag phase under the action of surface tension. At

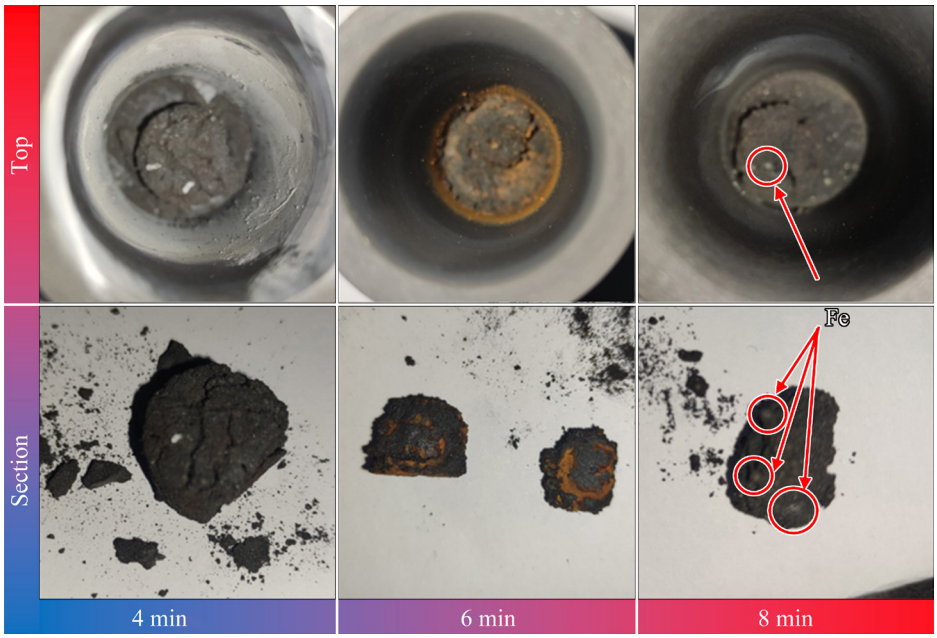

Fig. 8 Photographs of pellets at different melting time

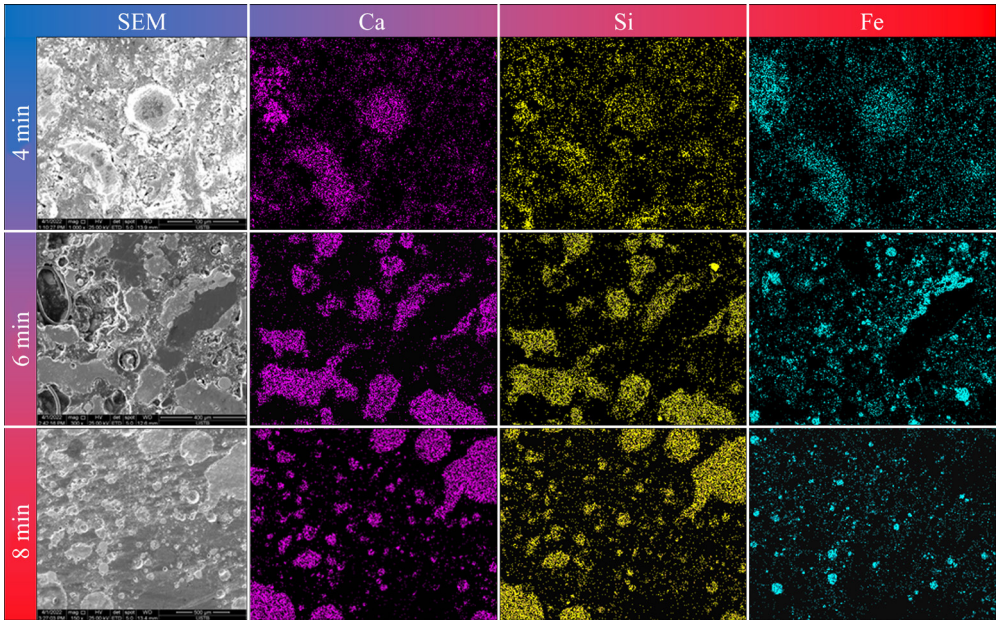

Fig. 9 SEM−EDS images of unmelted pellets at different melting time

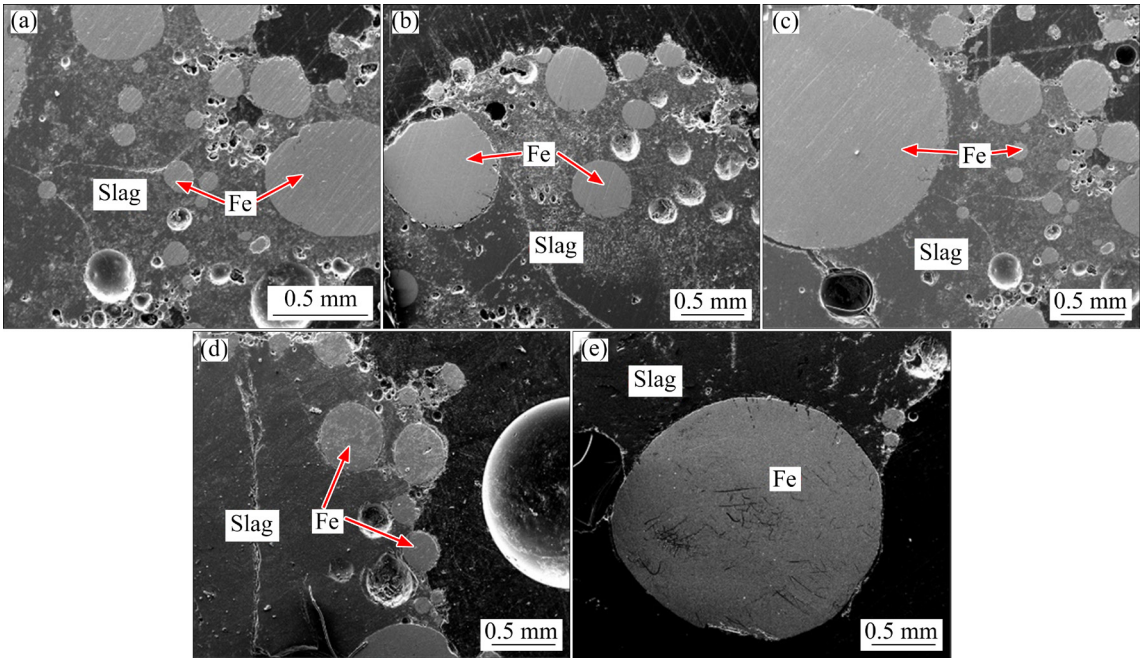

Fig. 10 SEM images of metal−slag interface at different melting time: (a) 5.0 min; (b) 7.5 min; (c) 10.0 min; (d) 12.5 min; (e) 15.0 min

10.0 min (Fig. 10(c)), the number of Fe droplets with a diameter less than 100 μm and Fe droplets at the metal−slag interface increased. This might be because the settling of the Fe droplets present in the slag phase had a diameter less than 100 μm on the metal−slag interface. At 12.5 min (Fig. 10(d)), the number of Fe droplets present at the metal−slag interface decreased, and they were distributed at the edge of the slag phase. At 15.0 min (Fig. 10(e)), the number of Fe droplets at the metal−slag interface was reduced further. This was because of the completion of the growth and sedimentation process of Fe droplets in the slag phase at 15.0 min, and only a small number of Fe droplets existed at the metal−slag interface, which did not completely enter the iron bath. Fe droplets with diameters less than 1000 μm (Fig. 10(e)) were present on the metal−slag interface at 15.0 min, which indicated that the separation of slag and iron under this experimental condition required a melting time

longer than 15.0 min. According to previous reports [27] and our study, it was speculated that the separation of Fe droplets in the slag phase was not completed in 15.0 min.

To study the process of Fe droplet growth in the slag phase and elucidate the iron droplet growth characteristics, the slag phase after the reaction was analyzed using an XCT. The XCT scan results of the slag phase at melting time of 10.0 min are shown in Fig. 11. The overall scan results of the slag phase in Fig. 11(a) showed that the colored spheres were the Fe droplets having different diameters present in the slag phase. The pink Fe droplets in Fig. 11(b) represented the pink Fe droplets in Fig. 11(a), and the silver Fe droplets in Fig. 11(b) represented the Fe droplets of other colors in Fig. 11(a).

As shown in Fig. 11, most of the iron droplets present in the slag phase at 10.0 min had a diameter ranging from 10 to 200 μm, and there were only a small number of Fe droplets with diameter >1000 μm. The average diameter of Fe droplets in the slag phase was 62 μm, and the maximum diameter was 3800 μm (the pink droplets in Fig. 11(b)). Also, Fig. 11(a) showed that the Fe droplets with a diameter <200 μm were mainly distributed at the upper side of the slag phase, while the Fe droplets with a diameter >1000 μm were mainly distributed on the lower side of the slag phase that was close to the metal−slag interface, and the Fe droplets with the largest diameter were found at the metal−slag interface. This was because a lot of the iron oxides in the pellet were reduced at 10.0 min, and the reduced Fe droplets in the slag phase moved toward the iron bath, obeying Stokes Law [28,29]. The Fe droplets having large diameters were the first to reach the metal−slag interface and undergo metal−slag separation. The Fe droplets collided with each other and grew during their downward movement. The pink Fe droplet in Fig. 11(b) was an iron droplet with a diameter >1000 μm formed by the combination of several Fe droplets of different diameters.

The XCT images of the slag phase at different melting time are shown in Fig. 12. It was found that the iron droplets present in the slag phase had a diameter ranging from 50 to 500 μm, and their average diameter was 100 μm at 12.5 min. The Fe droplets present in the slag phase gathered together, which resulted in an increase in the average diameter of Fe droplets during the span of melting time between 10.0 and 12.5 min. At 15.0 min, the iron droplets present in the slag phase had a diameter ranging from 50 to 100 μm, and their average diameter was 89 μm. This occurred because the large-diameter iron droplets had finished the separating process into the iron bath, while the remaining iron droplets in the slag phase had a smaller diameter. This was inconsistent with the electron microscope scan results and occurred because the small diameter droplets of iron did not reach the metal−slag interface and were not observed under the electron microscope.

From the analysis results of the XCT scan, it was found that the average diameter of Fe droplets in the slag phase initially increased up to 12.5 min and then decreased. However, the iron droplet coalescence was only qualitatively described without being interpreted quantitatively. Thus, the iron droplet sphericity was used to indicate whether the

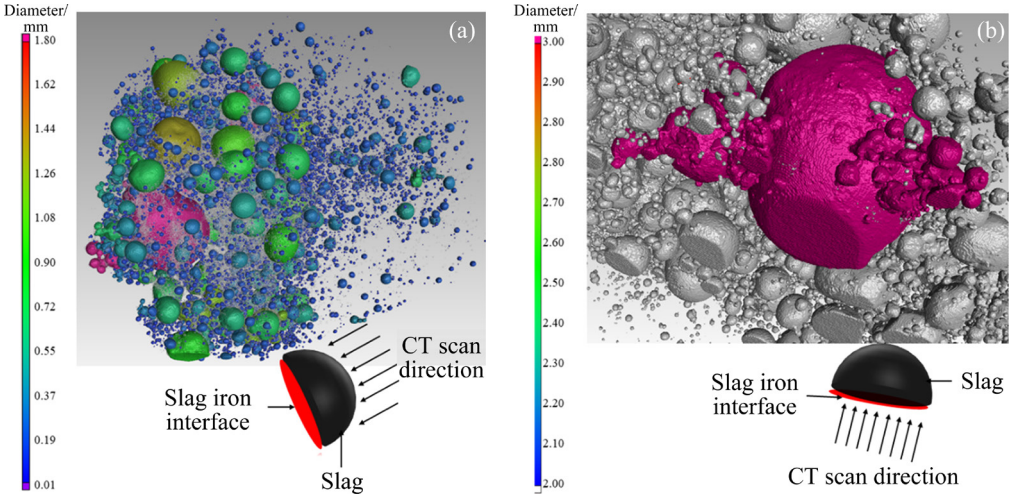

Fig. 11 XCT image of slag phase (a) and partially enlarged view (b) at melting point of 10 min

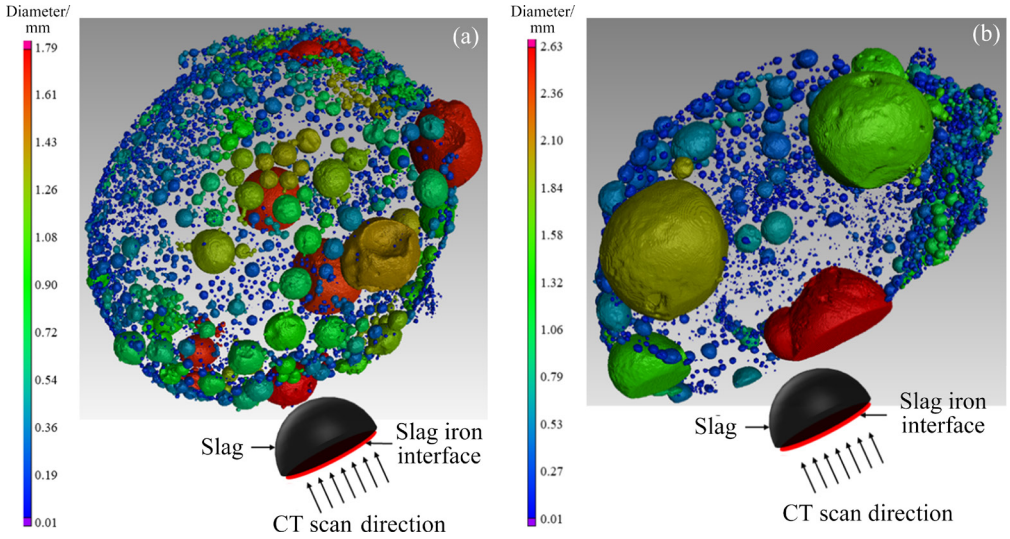

Fig. 12 XCT images of slag phase at different melting time: (a) 12.5 min; (b) 15.0 min

droplet aggregated and grew. The sphericity of Fe droplets was calculated using the formula as follows:

$$S_p = \frac{A_s}{A_d} \times 100\% \quad (10)$$

where S_p is the sphericity of Fe droplets, A_s is the surface area of the sphere of the same volume, and A_d is the surface area of the defective sphere.

In this study, it was found that when the iron droplet sphericity was ≥65%, the iron droplet was in an independent state, i.e., the iron droplet did not aggregate with other Fe droplets. When the iron droplet sphericity was <65%, the iron droplet aggregated with other Fe droplets, and the smaller the sphericity was, the more complicated the coalescence situation was. The sphericity and diameter of Fe droplets in the slag were correlated at different melting time, and the results are shown in Fig. 13. As shown in Fig. 13, most of the Fe droplets with sphericity >65% had a diameter <100 μm. At 10.0 min, a large number of Fe droplets with diameters ranging from 500 to 1000 μm had sphericity ranging from 63% to 67%, while the number of these Fe droplets with sphericity ranging from 63% to 67% and a diameter from 500 to 1000 μm decreased at 15.0 min. This indicated that the Fe droplets with large diameters completed the separation process with an increase in melting time, while the Fe droplets with small diameters accumulated and grew to form Fe droplets with a low sphericity and a large diameter. It was found that the distribution of iron droplet sphericity versus diameter at different reaction time followed a quadratic function. The distribution was aligned more closely to the quadratic function with an increased reaction time.

The Fe droplets were considered to be incompressible fluids before and after coalescence, with no change in their density. For the continuous flow field in the main region of the slag phase, it was the low Reynolds number Stokes laminar flow part, so the inertial force on the Fe droplets was neglected. The settling velocity of the iron droplet obeyed the Stokes Law, and the Stokes theorem was used in the description of the iron droplet motion. The velocity of iron droplet motion satisfied Eq. (11):

$$u_s = \frac{(\rho_d - \rho_c) g d^2}{18 \mu} \quad (11)$$

where u_s is the terminal velocity of droplet settling or floating, which is the iron droplet settling velocity (m/s), ρ_d is the dispersed phase droplet density, which is the iron droplet density (kg/m^3), ρ_c is the continuous-phase fluid density, which is the slag density (kg/m^3), g is the gravitational acceleration (9.80 m/s^2), d is the droplet diameter, which is the iron droplet diameter (m), and μ is the continuous phase kinetic viscosity, which is the slag phase kinetic viscosity (Pa·s).

The Stokes theorem (Eq. (11)) shows that when there is a density difference between slag and iron, the terminal settling rate of Fe droplets in the slag phase is proportional to the quadratic of the iron droplet diameter. The settling time of Fe droplets in the slag phase, i.e., the time required for

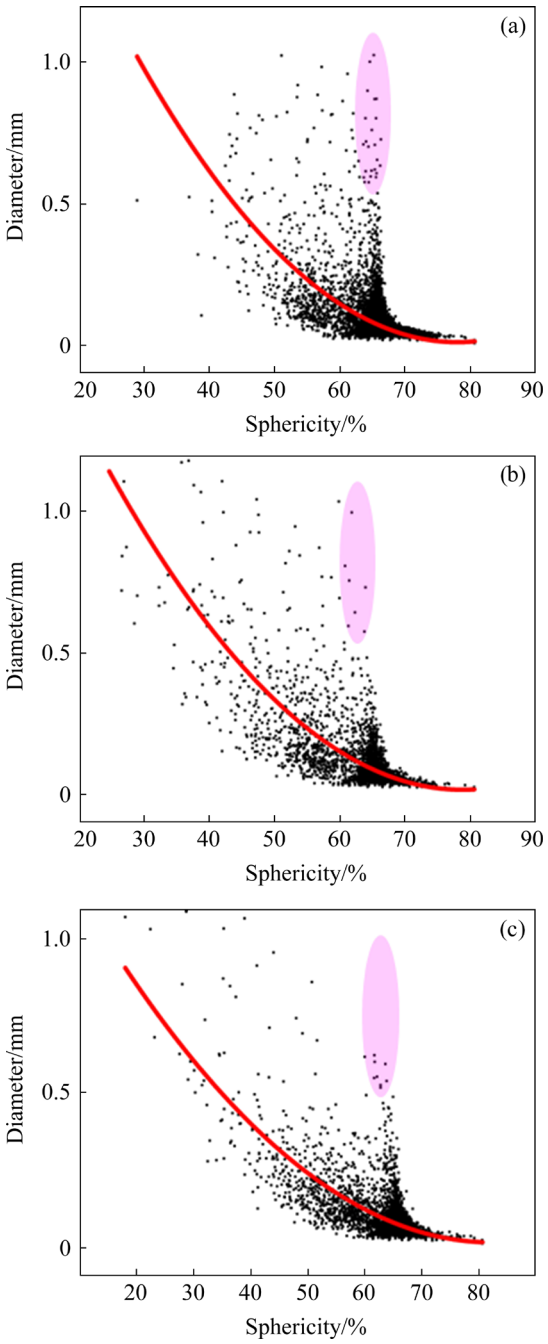

Fig. 13 Relationship between sphericity and diameter of Fe droplets at different melting time: (a) 10.0 min; (b) 12.5 min; (c) 15.0 min

metal−slag separation (t) satisfies Eq. (12):

$$t=l/u_s \tag{12}$$

where l is the thickness of the slag phase (m).

According to the spheroid volume formula, the diameter of two iron droplets with the same diameter aggregated was calculated to form a new iron droplet with a 26% greater diameter than the original single iron droplet diameter. Assuming that the time for the iron droplet to grow was negligible, from Eqs. (11) and (12), it was found that the settling time required for two Fe droplets of the same diameter after coalescence was 37% shorter than that before coalescence. The μ of this slag system was calculated according to FactSage 8.0. The ρ_d, ρ_c, and l were calculated theoretically and incorporated into Eqs. (11) and (12). The relationship between the time required for metal−slag separation and iron droplet diameter was derived, and the results are shown in Fig. 14. As shown in Fig. 14, the iron droplets with a larger diameter required a shorter time for separation. And the time required to separate iron droplets with a diameter <17 μm was >3600 s. The separation of iron droplets with a diameter <30 μm required 900 s, which was inconsistent with the results in Fig. 13. These inconsistencies occurred because of the following reasons: (1) Stokes Law ignored the coalescence behavior of iron droplets, (2) the reaction time and metal−slag separation time were inconsistent, and (3) the calculation process ignored the effect of ferrostatic pressure on the resistance of iron droplet aggregation and melt−slag separation.

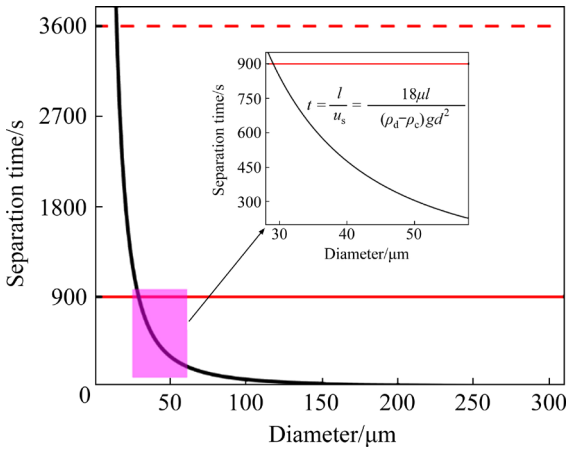

Fig. 14 Relationship between iron droplet diameter and metal−slag separation time

3.4 Mechanism of melting reduction for EAFD

To summarize the results of the experiments, a preliminary model of the reduction and melting separation of Zn-containing EAFD under iron bath conditions was established. The reduction and melting separation processes of pellets under iron bath conditions were divided into two parts: (1) Zn/Fe reduction and (2) metal−slag separation. This differed from the results of previous studies [30]. In this study, the two processes of reduction

and melting separation were only behaviorally distinguished, but there was a certain degree of temporal and spatial overlap between reduction and melting separation. In the reduction process, when the pellet was heated in the iron bath, its surface was the first to reach the temperature at which ZnO reacted with C, and eventually, ZnO was removed from the pellet surface. As the reduction time increased, the rate of ZnO reduction reaction increased with the internal temperature of the pellet, and ZnO was completely removed in a short time. Also, FeO in the pellet was partially reduced to metallic Fe, and other materials that did not undergo reduction reactions were slagged to form a liquid slag. After the formation of the liquid slag, it floated on the surface of the iron bath under the action of buoyancy. The presence of liquid slag facilitated the carburization reaction between Fe and C [31], which lowered the melting point of metallic Fe and led to the formation of Fe droplets. As the reduction time continued to increase, the pellet melted completely, and the liquid slag was laid flat on the surface of the iron bath. After the completion of the reduction reaction, a large amount of solid C was present in the slag phase, and the viscosity of the slag phase largely led to the blurring of the metal−slag interface.

The metal−slag separation process can be divided into four steps. During the first step, the pellet was heated under the iron bath conditions, which resulted in the formation of the liquid slag phase. The second step involved the carburization reaction between Fe and C. Fe in the slag phase followed the Brownian motion for a very short time, resulting in the formation of fine Fe droplets. But Fe droplets did not settle [32]. In the third step, the Fe droplets with larger diameters floated in the slag phase. When the role of Brownian motion blurred and the Marangoni motion became dominant, the Fe droplets aggregated and grew [33−35]. During the fourth step, the diameter of iron droplets increased further and settled in the slag phase, and its settling rate followed Stokes Law. The Fe droplets in the settling process grew continuously and accelerated the decline until they were finally separated from the slag phase into the iron bath. Due to the ferrostatic pressure, the time of aggregation of Fe droplets and their entry into the iron bath grew. The reduction and fusion processes are shown in Fig. 15.

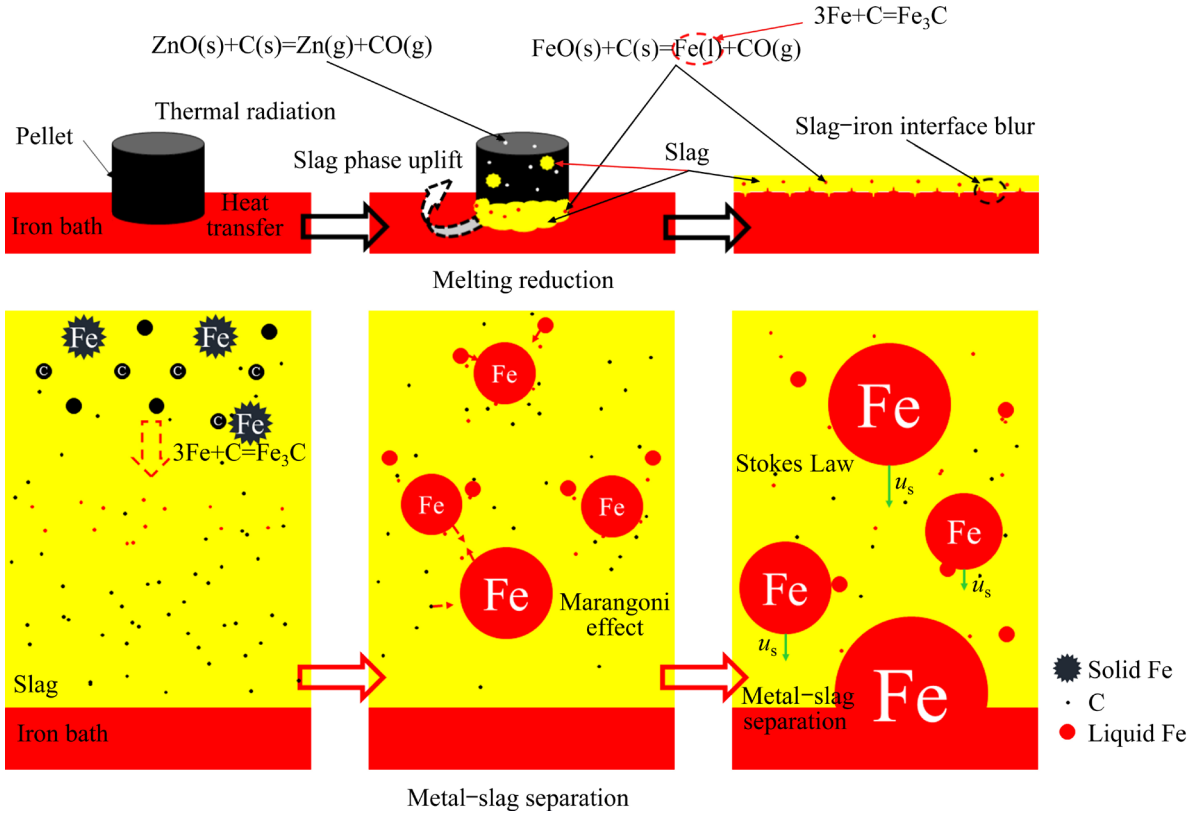

Fig. 15 Illustrative diagram of reaction mechanism of melting reduction and metal−slag separation

4 Conclusions

(1) Under the iron bath conditions, the ZnO removal rate in the pellet reached more than 99% at melting time of 5.0 min, and a small amount of Zn in the pellet was detected after 10.0 min of melting. The metal−slag separation was incomplete after 15.0 min of melting.

(2) Due to compositional fluctuations and temperature gradients, initially, liquid slag was formed at the bottom of the pellet and locally within the pellet. Then, the pellet around the liquid slag underwent a slagging reaction and fused with the liquid slag. Finally, the whole pellet melted completely.

(3) Sphericity was proposed as a criterion for judging the coalescence of iron droplets in pellets. If the sphericity of iron droplets is ≥65%, they exist alone; otherwise, they accumulate and grow. The number of iron droplets with diameter >500 μm and sphericity >65% decreased with the increase in melting time. After melting for 15.0 min, a large number of iron droplets still accumulated and grew, and the metal−slag separation was not completed.

(4) The metal−slag melting separation model was divided into four steps. The first step involved the formation of liquid slag. In the second step, iron droplets appeared and grew under the action of Brownian motion. During the third step, further coalescence of iron droplets occurred under the Marangoni effect. In the final step, iron droplets dropped, continued to aggregate with other iron droplets, and grew. The rate of descent was determined by Stoke's theorem, and metal−slag separation was completed.

CRediT authorship contribution statement

Chao YANG：Conceptualization, Methodology, Writing − Original Draft; **Xue-feng SHE:** Formal analysis, Resources, Writing − Review & editing; **Ru-yi WANG:** Validation, Investigation; **Jing-song WANG:** Supervision, Project administration; **Qing-guo XUE:** Funding acquisition, Data Curation.

Declaration of competing interest

The authors declare that they have no known competing financial interests or personal relationships that could have appeared to influence the work reported in this paper.

Acknowledgments

This work was supported by the National Key R&D Program of China (No. 2019YFC1905703), and Provincial Science and Technology Plan Projects in Guangdong Province, China (No. GDKJ2020002).

References

[1] GRILLO F, COLETI J, ESPINOSA D, OLIVEIRA J, TENÓRIO J. Zn and Fe recovery from electric arc furnace dusts [J]. Materials Transactions, 2014, 55: 351−356.

[2] LIN Xiao-long, PEMG Zhi-wei, YAN Jia-xing, LI Zhi-zhong, HWANG Jiann-yang, ZHANG Yuan-bo, LI Guang-hui, JIANG Tao. Pyrometallurgical recycling of electric arc furnace dust [J]. Journal of Cleaner Production, 2017, 149: 1079−1100.

[3] LOAIZA A, CIFUENTES S, COLORADO H A J C, MATERIALS B. Asphalt modified with superfine electric arc furnace steel dust (EAF dust) with high zinc oxide content [J]. Construction and Building Materials, 2017, 145: 538−547.

[4] MACHADO J G, BREHM F A, MORAES C A M, dos SANTOS C A, VILELA A C F, da CUNHA J B M. Chemical, physical, structural and morphological characterization of the electric arc furnace dust[J]. Journal of Hazardous Materials, 2006, 136: 953−960.

[5] CHEN W S, SHEN Y H, TSAI M S, CHANG F C. Removal of chloride from electric arc furnace dust [J]. Journal of Hazardous Materials, 2011, 190: 639−644.

[6] LI Chung-lee, TSAI Min-shing. A crystal phase study of zinc hydroxide chloride in electric-arc-furnace dust [J]. Journal of Materials Science, 1993, 28: 4562−4570.

[7] QUIJORNA N, de PEDRO M, ROMERO M, ANDRÉS A. Characterisation of the sintering behaviour of Waelz slag from electric arc furnace (EAF) dust recycling for use in the clay ceramics industry [J]. Journal of Environmental Management, 2014, 132: 278−286.

[8] IWASE G, OKUMURA K. Nonisothermal investigation of reaction kinetics between electric arc furnace dust and calcium chloride under carbon-containing conditions [J]. ISIJ International, 2021, 61: 2483−2489.

[9] KUL M, OSKAY K O, ŞİMŞİR M, SÜBÜTAY H, KIRGEZEN H. Optimization of selective leaching of Zn from electric arc furnace steelmaking dust using response surface methodology [J]. Transactions of Nonferrous Metals Society of China, 2015, 25(8): 2753−2762.

[10] WANG Hong-jun, LIU Zhi-yong, LIU Zhi-hong, LI Yu-hu, LI Si-wei, ZHANG Wen-hai, LI Qi-hou. Leaching of iron concentrate separated from kiln slag in zinc hydrometallurgy with hydrochloric acid and its mechanism [J]. Transactions of Nonferrous Metals Society of China, 2017, 27(4): 901−907.

[11] ANTREKOWITSCH J, RÖSLER G, STEINACKER S. State of the art in steel mill dust recycling [J]. Chemie Ingenieur Technik, 2015, 87: 1498−1503.

[12] VOGELBACHER M, KELLER S, ZEHM W, MATTHES J. Advanced methods for kiln-shell monitoring to optimize the waelz process for zinc recycling [J]. Processes, 2021, 9: 1062−1077.

[13] MUICA V T, OZUNU A, TÖRÖK Z. Comparative life cycle impact assessment between the productions of zinc from conventional concentrates versus waelz oxides obtained from slags [J]. Sustainability, 2021, 13(2): 580−597.

[14] WANG Jie, ZHANG Ying-yi, CUI Kun-kun, FU Tao, GAO Jian-jun, HUSSAIN S, ALGARNI T S. Pyrometallurgical recovery of zinc and valuable metals from electric arc furnace dust—A review [J]. Journal of Cleaner Production, 2021, 298: 126788−126811.

[15] GRUDINSKY P, ZINOVEEV D, DYUBANOV V, KOZLOV P. State of the art and prospect for recycling of Waelz slag from electric arc furnace dust processing [J]. Inorganic Materials: Applied Research, 2019, 10: 1220−1226.

[16] BRANCA T A, COLLA V, ALGERMISSEN D, GRANBOM H, MARTINI U, MORILLON A, PIETRUCK R, ROSENDAHL S. Reuse and recycling of by-products in the steel sector: Recent achievements paving the way to circular economy and industrial symbiosis in Europe [J]. Metals, 2020, 10: 345−363.

[17] MAŁECKI S, GARGUL K, WARZECHA M, STRADOMSKI G, HUTNY A, MADEJ M, DOBRZYŃSKI M, PRAJSNAR R, KRAWIEC G. High-performance method of recovery of metals from EAF dust—Processing without solid waste [J]. Materials, 2021, 14: 6061−6073.

[18] PICKLES C. Thermodynamic analysis of the separation of zinc and lead from electric arc furnace dust by selective reduction with metallic iron [J]. Separation and Purification Technology, 2008, 59: 115−128.

[19] LUNDKVIST K, ROSENDAHL S, NYMAN F, BÖLKE K, GUSTAVSSON L, SÖDERSTRÖM D, WEDHOLM A. Oxyfines technique for upgrading zinc containing blast furnace sludge—Part 1: Pilot trials [J]. Metals, 2020, 10: 1468−1481.

[20] SHE Xue-feng, WANG Jing-song, WANG Guang, XUE Qing-guo, ZHANG Xin-xin. Removal mechanism of Zn, Pb and alkalis from metallurgical dusts in direct reduction process [J]. Journal of Iron and Steel Research (International), 2014, 21: 488−495.

[21] NAKAYAMA M. EAF dust treatment for high metal recovery [J]. SEAISI Quart, 2012, 41: 22−26.

[22] LIU Xing-le, LIU Zheng-jian, ZHANG Jian-liang, XING Xiang-dong. Recovery of iron and zinc from blast furnace dust using iron-bath reduction [J]. High Temperature Materials and Processes, 2019, 8: 767−772.

[23] ZHU Zi-zong, SHEN Yong-ling, QIAO Sheng-pu. Separating Zn and Pb from BF dust by iron-bath process [J]. Journal of Iron and Steel Research, 2002, 14: 1−5.

[24] LEUCHTENMÜLLER M, LEGERER C, BRANDNER U, ANTREKOWITSCH J. Carbothermic reduction of zinc containing industrial wastes: A kinetic model [J]. Metallurgical and Materials Transactions B, 2021, 52: 548−557.

[25] FERREIRA F B, FLORES B D, OSÓRIO E, VILELA A C F. Carbothermic reduction of electric arc furnace dust via thermogravimetry [J]. REM−International Engineering Journal, 2018, 71: 411−418.

[26] QIN Ya-guang, GU De-sheng, HU Jian-hua, YANG Dong-jie, MA Shao-wei, BAI Xin, FENG Chun-di. Microscale deformation behavior of sandstone mineral particles based on XCT scanning [J]. Transactions of Nonferrous Metals Society of China, 2022, 32(4): 1261−1276.

[27] HE Mei-le, CHEN Min, WANG Nan, LI Chuan-fu. Sedimentation behavior of liquid iron droplets during smelting reduction of converter slag by considering the coalescence of droplets [J]. ISIJ International, 2019, 59: 973−980.

[28] DEY S, ALI S Z, PADHI E. Terminal fall velocity: The legacy of Stokes from the perspective of fluvial hydraulics [J]. Proceedings, Mathematical, Physical, and Engineering Sciences, 2019, 475(2228): 20190277−20190310.

[29] FRISING T, NOIK C, DALMAZZONE C, PEYSSON Y, PALERMO T. Contribution of the sedimentation and coalescence mechanisms to the separation of concentrated water-in-oil emulsions [J]. Journal of Dispersion Science and Technology, 2008, 29: 827−834.

[30] WANG Guang, XUE Qing-guo, WANG Jing-song. Reduction and melting separation mechanism of boron-bearing iron concentrate/coal composite pellet [J]. Journal of Iron and Steel Research (International), 2018, 25: 310−319.

[31] PARK J O, JEONG I H, JUNG S M, SASAKI Y. Metal−slag separation behaviors of pellets consisted of iron, graphite and $CaO-Al_2O_3$ based slag powders [J]. ISIJ International, 2014, 54: 1530−1538.

[32] FERGUSON J, SCHULTZ B F, ROHATGI P K, KIM C S. Impact of Brownian motion on the particle settling in molten metals [J]. Metals and Materials International, 2014, 20: 747−755.

[33] SCRIVEN L, STERNLING C. The marangoni effects [J]. Nature, 1960, 187: 186−188.

[34] STERNLING C, SCRIVEN L. Interfacial turbulence: Hydrodynamic instability and the Marangoni effect [J]. AIChE Journal, 1959, 5: 514−523.

[35] WECKER C, SCHULZ A, HEINE J, BART H J, KENIG E Y. Droplet formation—A numerical investigation of liquid-liquid systems with consideration of Marangoni convection [J]. International Journal of Heat and Mass Transfer, 2022, 188: 122465−122478.

铁浴条件下电炉粉尘球团的熔融与分离行为

杨 超[1]，佘雪峰[1]，王如意[2]，王静松[1]，薛庆国[1]

1. 北京科技大学 钢铁冶金新技术国家重点实验室，北京 100083；
2. 宝山钢铁股份有限公司 技术中心，上海 201900

摘 要：为了提高对含锌电弧炉粉尘(EAFD)的利用效率，实验研究 EAFD 球团在铁浴条件下的还原熔化行为。定义铁液滴球形度作为判断其凝聚的标准，然后探讨铁液滴直径和球形度之间随时间变化的关系。根据实验最终建立 EAFD 颗粒的熔化和分离行为。结果表明，在铁浴条件下，EAFD 球团的 Zn 去除率在 5.0 min 时达到 99%以上，但在 15.0 min 时金属渣分离还没有完成。由于成分的波动，在 EAFD 球团中形成几个区域的液态渣，然后液态渣不断增加，直到球团完全熔化。球形度>65%、直径>500 μm 的 Fe 液滴的数量随着时间的推移而减少，大直径的 Fe 液滴先完成分离。渣铁分离过程如下：在布朗运动下 Fe 液滴在渣中形成，之后 Fe 液滴直径在马兰戈尼效应下增加，Fe 液滴在渣中下降速度符合斯托克斯定律。

关键词：电炉粉尘；铁浴；球团融化；渣铁分离

(Edited by Bing YANG)